


Development of a setup to characterize capillary liquid bridges between liquid infused surfaces


Cite as: AIP Advances 12, 015120 (2022); <https://doi.org/10.1063/5.0072548>

Submitted: 02 December 2021 • Accepted: 13 December 2021 • Published Online: 19 January 2022

 Sarah J. Goodband,  Halim Kusumaatmaja and  Kislun Voïtchovsky

COLLECTIONS

 This paper was selected as Featured

 This paper was selected as Scilight



View Online



Export Citation



CrossMark

ARTICLES YOU MAY BE INTERESTED IN

[Blueprints offer replicable method to measure capillary liquid bridges](#)


Scilight 2022, 031105 (2022); <https://doi.org/10.1063/10.0009363>

[Symmetry-dependent electronic structure transition in graphether nanoribbons](#)

AIP Advances 12, 015118 (2022); <https://doi.org/10.1063/5.0077309>

[Validation of theoretical analysis of surface bending strain in polymer films by surface-labeled grating method](#)

AIP Advances 12, 015324 (2022); <https://doi.org/10.1063/5.0077846>



Call For Papers!

AIP Advances

SPECIAL TOPIC: Advances in Low Dimensional and 2D Materials

Development of a setup to characterize capillary liquid bridges between liquid infused surfaces

Cite as: AIP Advances 12, 015120 (2022); doi: 10.1063/5.0072548

Submitted: 2 December 2021 • Accepted: 13 December 2021 •

Published Online: 19 January 2022



Sarah J. Goodband,  Halim Kusumaatmaja,  and Kislun Voïtchovsky 

AFFILIATIONS

Department of Physics, Durham University, Durham DH1 3LE, United Kingdom

^{a)}halim.kusumaatmaja@durham.ac.uk

^{b)}Author to whom correspondence should be addressed: kislun.voitchovsky@durham.ac.uk

ABSTRACT

Capillary liquid bridges are ubiquitous in nature and are present in many industrial processes. In order to model their behavior, it is essential to develop suitable experimental tools that are able to characterize the bridges' geometry and the associated capillary force they induce on the contacting surfaces. While many existing setups are capable of characterizing capillary bridges formed between conventional surfaces, quantitative measurements on smart surfaces such as liquid infused surfaces remain challenging. These surfaces typically exhibit weak contact line pinning and contact angle hysteresis, resulting in unusually small changes in the capillary force they exert upon extension or compression of the bridge. Although it is precisely these properties that drive the interest into liquid infused surfaces, they render experimental characterization challenging when compared to non-infused surfaces. Here, we tackle this issue by developing a relatively inexpensive setup capable of measuring capillary forces with sensitivity in the micronewton range while quantifying the bridge's geometry. The setup is fully motorized and can vary the relative position of the contacting surfaces while maintaining synchronous force and geometry measurements. We also present a new analysis software developed to retrieve the relevant geometrical parameters of the bridge from optical observations while minimizing errors and noise. Using example surfaces, we demonstrate the setup's capabilities, including for bridges between liquid infused surfaces.

© 2022 Author(s). All article content, except where otherwise noted, is licensed under a Creative Commons Attribution (CC BY) license (<http://creativecommons.org/licenses/by/4.0/>). <https://doi.org/10.1063/5.0072548>

I. INTRODUCTION

Capillary liquid bridges (CLBs) are created when a droplet of liquid forms a stable link between two surfaces, usually solids. In nature, countless examples of water based CLBs can be found, from the cohesive force holding soil and sandcastles together¹ to the adhesion of small animals and insects to surfaces,^{2–4} the function of our joints,⁵ and in several respiratory diseases.^{6,7} In technology and industrial applications, CLBs are also ubiquitous in processes such as soldering,^{8,9} lithography,¹⁰ oil recovery,¹¹ and cement drying,¹² with potential for medical processes such as stem cell and drug delivery.¹³

The behavior of CLBs is influenced by many environmental and physical factors as well as the fluid used to create the bridge. The exact shape of the CLB and the force it exerts on the contacting surfaces are determined by an interplay between the surface tension of the liquid, the shape of the surfaces, and the affinity between the liquid and the surfaces. Gravity also influences CLBs, but its effect only becomes noticeable at scales larger than the so-called capillary length

(about 2 mm for pure water). Given the importance of CLBs in science and technology, considerable research aims at modeling^{14–18} and experimentally characterizing their properties^{19–21} over a wide range of relevant conditions.

Experimentally, a variety of setups have been developed to explore CLBs stretched between parallel or non-parallel solid plates. At the nanoscale, force measurements typically rely on atomic force microscopy^{19,20} or similar devices.²¹ Nano-bridge sizes range from a few nanometers to hundreds of nanometers, and the associated capillary forces range from piconewton to tens of nanonewtons. Although highly precise spatially, such measurements do not allow for direct visualization for the CLB or characterization of its shape while being deformed. Asperities or chemical inhomogeneities of the surfaces can also dramatically affect the measurements which usually involve atomically flat, ideal surfaces that are not representative of most applications. In contrast, CLB measurements over the millimeter scale allow for direct visualization of the CLB evolution as the distance between surfaces changes.^{22–28} At that scale, capillary

forces are typically in the range of millinewtons^{22,23} and the effect of gravity may need to be taken into consideration depending on the particular system considered.²⁹ Given the relatively large size of such CLBs, the geometry and chemical properties of the surfaces can be well controlled on the relevant scale, including via the introduction of chemical patches,^{24,30} surface corrugations,³¹ or non-parallel geometries, such as spheres²³ and wedges.²⁵

While standard nanoscale and millimeter-sized “macroscale” measurements have enabled significant advances in the field, many phenomena involving CLBs fall in the in-between region, where capillary forces range between sub-micronewtons to hundreds of micronewtons. In this range, directly observing the CLB is usually still possible, but measuring the force it exerts on the contacting surfaces becomes challenging and requires bespoke experimental setups.³² Such setups are usually expensive, highly specialized, and unsuitable for routine measurements.

This gap is all the more problematic with the advent of liquid infused surfaces (LIS), where CLBs are only expected to induce micronewton force changes when extended, even at the millimeter scale. Since their discovery,^{33–35} LIS have enabled important development in the field of surface science and wetting, with important implications for surface capillary phenomena.³⁵ The interest in LIS is motivated by a wide range of technological applications from anti-fouling properties to anti-icing,^{36–38} antibacterial,^{39–41} self-healing,^{33,42} and anticorrosive properties.^{43,44} Simulations have captured some aspects of CLBs formed between LIS,¹⁴ but experimental studies are lagging behind, owing to the difficulties associated with such measurements.

In the present study, we develop a novel setup to study CLBs between parallel plates with improved force sensitivity, down to the micronewton range. The plates can be functionalized with any desired surface, making the system suitable for measurements on LIS. The setup, built from relatively inexpensive and commercially available parts, is fully motorized for relative displacements of the surfaces over several millimeters. It is versatile and can be easily adjusted to suit different geometrical configurations or work in specific environments. It can incorporate multiple cameras working simultaneously (here two) for more accurate measurements, and a bespoke software is developed to drive the experiments and subsequently analyze the data collected from the camera and the force sensor.

We illustrate the measurement capabilities of the setup by tracking the changes in force and geometry associated with the extension and the compression of CLBs between salinized glass surfaces and between planar LIS.

II. RESULTS AND DISCUSSION

Before describing in detail the setup developed, it is useful to briefly summarize some of the key details of typical measurements involving CLBs, including the observables necessary for quantitatively describing the CLB and the underlying theory.

A. Theory and background knowledge

1. Basic characteristics of CLBs

The main geometrical parameters used to describe CLBs are (1) the angles θ_1 and θ_2 formed by the liquid and the contacting surfaces,

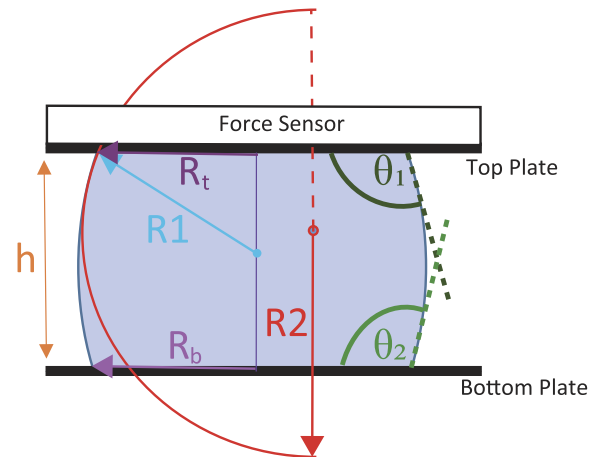


FIG. 1. Cartoon representation of a typical CLB between parallel surfaces. The CLB can be quantitatively described and modeled using the contact angles θ_1 and θ_2 formed by the liquid with each surface, the height h of the bridge (here the distance between the surfaces), the radii of contact R_t and R_b of the bridge with the top and bottom surfaces, respectively, and the curvature of the CLB surface obtained by two radii of curvature R_1 and R_2 taken orthogonally from each other. Here, the radii R_1 and R_2 are taken at the point of contact with the top plate, but they can, in principle, be taken anywhere on the bridge at equilibrium.

(2) the height h of the bridge, (3) the radii of contact R_t and R_b at the top and bottom surfaces, respectively, and (4) the radii of curvature R_1 and R_2 of the surface of the liquid bridge (Fig. 1). R_1 and R_2 are shown in Fig. 1 at the point of contact between the liquid bridge and the top contacting surface.

The CLB exerts a capillary force on the contacting surfaces. The magnitude and direction of this force depend on the specific geometry of the system. Gravity is also present, and its effect may have to be taken into consideration, depending on the size and volume of the CLB. In larger CLBs, the gravity-induced differential hydrostatic pressure between the top and the bottom of the CLB results in an asymmetric shape.

The geometrical parameters of the CLB can be related to its capillary force F . In the case where we can ignore gravity, the capillary force for a symmetric CLB between two identical parallel surfaces is given by^{45,46}

$$F = -2\pi\gamma R \sin(\theta) + \pi R^2 \gamma \left(\frac{1}{R_1} + \frac{1}{R_2} \right), \quad (1)$$

where γ is the surface tension of the liquid, and we have assumed $\theta_1 = \theta_2 = \theta$ and $R_t = R_b = R$ by symmetry. This equation assumes equilibrium and a CLB size well below the capillary number. When gravity becomes important, the CLB is no longer symmetric. In this case, the capillary force at the top plate can be expressed as

$$F_t = -2\pi\gamma R_t \sin(\theta_1) + \pi R_t^2 \gamma \left(\frac{1}{R_1} + \frac{1}{R_2} \right). \quad (2)$$

Here, the radii of curvature R_1 and R_2 are measured at the top plate. For the bottom plate, the magnitude of the capillary force includes an additional term due to gravity⁴⁵ and is given by

$$F_b = -2\pi\gamma R_t \sin(\theta_1) + \pi R_t^2 \gamma \left(\frac{1}{R_1} + \frac{1}{R_2} \right) + \rho g V, \quad (3)$$

where ρ is the density of the droplet solution, V is the CLB volume, and g is the acceleration of gravity. Alternatively, the capillary force for the bottom plate can be written in a form akin to Eqs. (1) and (2),

$$F_b = -2\pi\gamma R_b \sin(\theta_2) + \pi R_b^2 \gamma \left(\frac{1}{R_1} + \frac{1}{R_2} \right), \quad (4)$$

where the radii R_b , R_1 , and R_2 and contact angle θ_2 are all now measured at the bottom plate. Equations (1)–(3) can also describe capillary bridges on LIS when stationary and at equilibrium.

2. Practical experimental considerations and common issues

In a typical experimental measurement, the geometry of a CLB is tracked by a camera while a given parameter (here the distance h between the surfaces) changes continuously. The associated capillary force F experienced by one of the contacting surfaces is also measured. The CLB geometry is usually extracted from 2-dimensional video images of the bridge, which have to be synchronized with the force measurements.

Most experimental measurements face several challenges. One key problem stems from assuming symmetry and uniformity over the entire CLB. This is implicit as we use a 2D image to extract all the geometrical parameters (θ_1 , θ_2 , h , R_t , R_b , R_1 , and R_2) assumed to represent the bridge at equilibrium. For large CLBs, or CLBs experiencing pinning on the surface, this assumption may not be valid because the optical image may miss pinned points. However, the measured force is sensitive to such pinning points, resulting in a disagreement between the measured force and that calculated from the geometrical parameters. Liquid evaporation may lead to time-dependent changes in the force over longer measurements due to changes in the CLB's volume. Using larger CLBs can reduce the relative importance of evaporation effects but at the cost of needing to take into account gravity. Alternatively, CLBs can be made of liquids less susceptible to evaporation (e.g., water–glycerol mixture instead of pure water^{47,48}) and make use of a controlled environment (e.g., humidity and temperature^{49,50}).

3. Working with LIS

Measuring CLBs between LIS is more challenging for several reasons. First, the changes in capillary force as the CLBs are stretched are typically an order of magnitude lower than those for CLBs of the same size but involving non-LIS. Second, while LIS are of interest, precisely, for the absence of contact line pinning^{51,52} and the ability of droplets to roll off easily,³⁵ these properties render CLB measurements more challenging due to increased bridge mobility. Additionally, the liquid layer of the LIS (typically oil) can create a visible ridge around the CLB–LIS contact regions or may cloak the whole bridge,⁵³ rendering precise determination of θ more difficult (Fig. 2). The contact angle must then be approximated either by fitting the bridge edge and extrapolating the obscured region

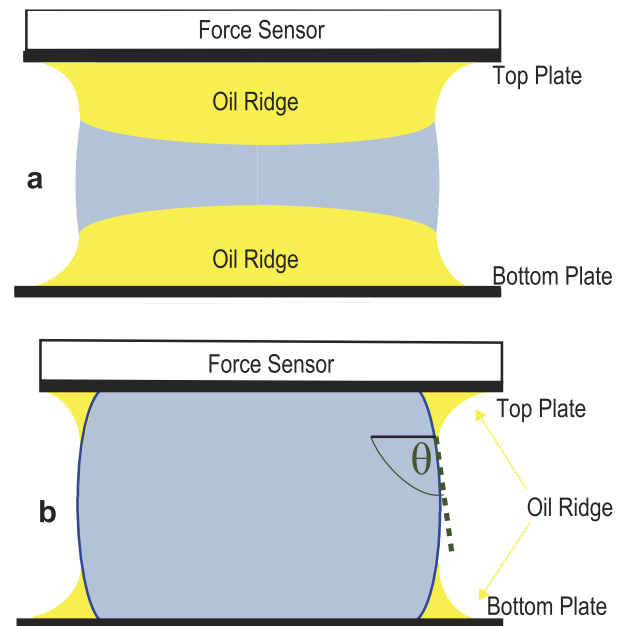


FIG. 2. Cartoon of a CLB between two LIS with an apparent oil ridge. (a) Oil ridges as seen in a camera image of the CLB. The oil ridges develop when thicker oil layers are used on the LIS, obscuring the contact angle of the bridge with the surface. (b) A section through the middle of the liquid bridge illustrates the situation from the perspective of the CLB geometrical characterization. The contact angle is approximated by taking the apparent contact angle measured at the three-phase contact line between the droplet, lubricant, and surrounding gas.¹⁸

[Fig. 2(b)] or by approximating the contact angle using geometrical arguments.¹⁸ When focusing on cases with small oil ridges, these two approximations converge to the same value. However, for larger oil ridges, their values can differ significantly, and it is important to employ consistent radii and contact angle definitions in Eqs. (1) and (2). For practical reasons, it is often convenient to define them at the droplet–lubricant–gas contact line.

The impact of the oil ridge on the measurements depends on the thickness of the LIS liquid layer, thus rendering the issue system dependent. The ridge may also impact the measurement of the curvature depending on which approximations are used, and its size can grow during the measurements (something that needs to be taken into account while studying changes in the contact angles). To overcome this issue, a solution with a dye dissolved in the droplet or the LIS liquid⁵⁴ can be used so as to highlight the contact line or contact angles. There is, however, some concern that dye molecules could affect the surface tension of the fluids and hence the contact angles measured.

B. Setup developed

The setup developed in this paper uses a standard design^{22–24} with one of the surfaces fixed and the other motorized and suspended to a high-precision force sensor. Cameras provide direct visualization of the CLB's geometry, with all pieces of hardware

controlled and synchronized using the same computer software. While several hardware and software aspects of the development improve on existing setups, the key improvement is the force sensitivity (accuracy to $4\ \mu\text{N}$), with demonstrated measurements on CLB between LIS. This improvement also entails some limitations, which are discussed in Sec. III.

1. Components and parts

The key building elements of the setup are a micronewton sensitive force cell (Novatech Measurements Limited, St Leonards on Sea, UK), a high-quality digital camera (IDS Imaging Development Systems GmbH, Obersulm, Germany) and motorized stages (Thorlabs LTD., Ely, UK), all interfaced, synchronized and controlled using LabVIEW (National Instruments, Austin, TX, USA). Each item is listed in Table I with the key elements labeled as “essential” while optional improvements are labeled “optional.”

The different items are assembled as shown in Fig. 3. The force sensor (Novatech, F329 Deci-Newton Load cell), mounted on the vertical motorized stage (Thorlabs, KVS30/M), can operate symmetrically in both traction and compression. We opted for a top position with the sensor suspended to a custom-made holder. Both the top and bottom stages can be manually adjusted to change the sample position while loading, including the relative tilt angle (usually around 0.5°) of the bottom plate. This is useful to apply minute corrections of the plate parallelism. Removable plates can be screwed into the force sensor, allowing for different surfaces to be easily and stably mounted. Suspending the force sensor has a number of benefits: it protects against liquid ingress while using very mobile droplets, prevents oil shed during longer experiments or due to droplet rolling contaminating the sensor, and gives the sensor some protection from the user, who is less likely to knock or touch it. In this way, the sensor is only ever contacted by droplets that are

TABLE I. List of the different parts used to create the CLB measurement setup. All prices are correct as of the time of purchase. Some basic parts were made in-house.

Part name and model	Provider	Importance for setup
<i>Base</i>		
Nexus B4560A breadboard, $450 \times 600 \times 60\ \text{mm}^3$, M6 \times 1.0 mounting holes	Thorlabs	Essential
<i>Z-stage mounting system</i>		
Lab clamp stands	Various	Essential
KVS30/M—Kinesis [®] 30 mm vertical translation stage, M6 and M4 tapped holes	Thorlabs	Essential
GNL10/M-Z8—large motorized goniometer, 25.4 mm distance to point of rotation, $\pm 8^\circ$, metric	Thorlabs	Optional
MT1/M-Z8—12 mm (0.47") one-axis motorized translation stage, M6 taps	Thorlabs	Optional
KDC101—K-cube brushed DC servo motor controller	Thorlabs	Essential
<i>Camera system</i>		
MVL6X12Z—6.5 \times zoom lens with 12 mm fine focus	Thorlabs	Essential
MVL6X05L—0.5 \times magnifying lens attachment for 6.5 \times zoom lens	Thorlabs	Essential
High sensitivity digital camera UI-3880CP-M-GL Rev. 2	IDS	Essential
Custom extension tube for camera mounting	In-house	Essential
PT102/M—right-angle bracket for PT series translation stages	Thorlabs	Essential
PT1/M—25.0 mm translation stage with standard micrometer, M6	Thorlabs	Essential
Lab jack	Various	Essential
<i>Force sensor and mounting</i>		
P300/M - $\varnothing 1.5''$ mounting post, M6, 300 mm	Thorlabs	Essential
C1511/M - $\varnothing 1.5''$ post mounting clamp, $63.5 \times 63.5\ \text{mm}^2$, metric	Thorlabs	Essential
DSC USB Load cell Digitizer	Novatech	Optional
F329 Deci-Newton Load cell	Novatech	Essential
Custom force sensor mounting plate	In-house	Essential
PT1/M—25.0 mm translation stage with standard micrometer, M6	Thorlabs	Essential
Easyfix blue zinc-plated hose clips	Screwfix	Essential
<i>Illumination</i>		
ICEFIRE T70 torch LED	Amazon	Essential
Custom diffusing screen	Custom	Essential
<i>Second camera setup</i>		
Dino-lite AM7915MZT—EDGE	Dino-lite	Optional
Lab clamp stands	Various	Optional

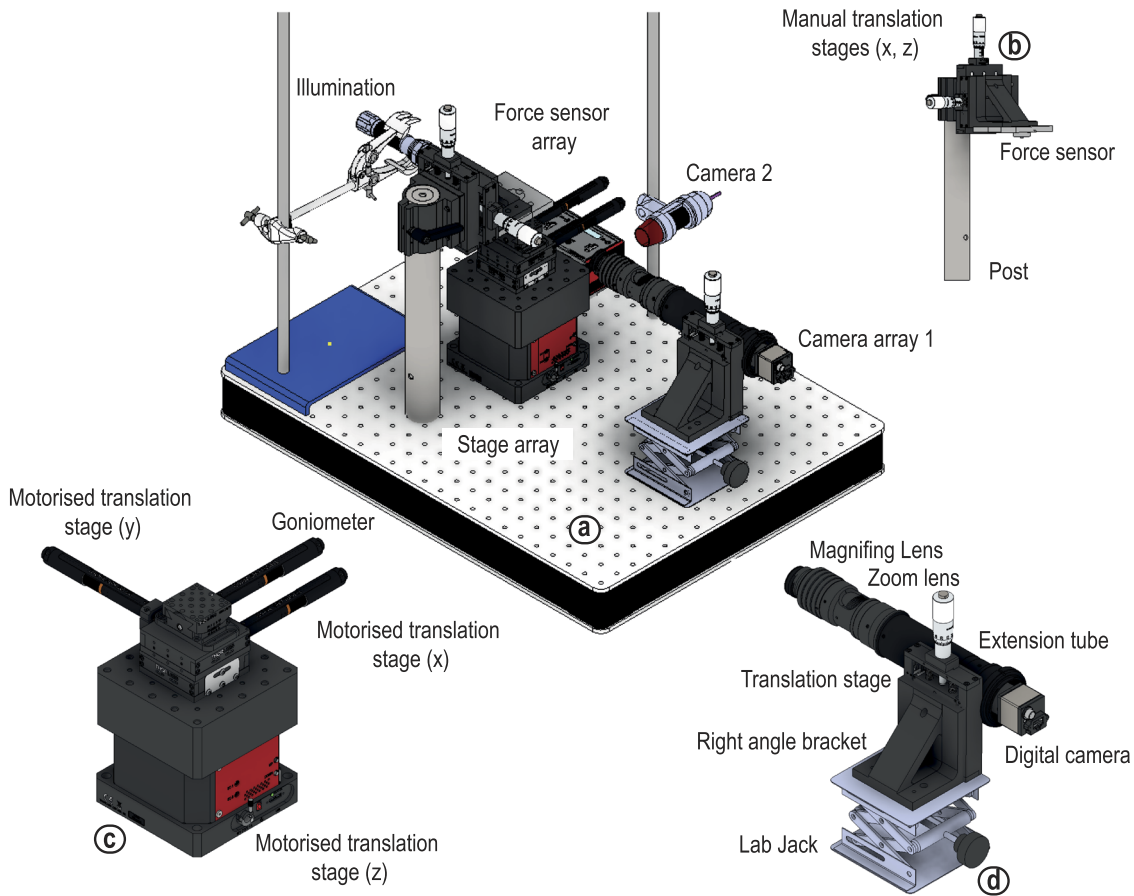


FIG. 3. Technical drawing of the developed setup. (a) The fully assembled setup is shown without any of the wires to aid visualization. The main components are magnified in the edges with full labeling (b)–(d). (b) The force sensor is attached to a custom holder and is suspended above the stage array. There are manual stage controls attached to the force sensor mount to assist with the setup. (c) The x, y, z, and tilt stages are all motorized. (d) The main camera (UI) has an adjustable lab jack and a manual stage for fine adjustments to the setup. The second camera (Dino-lite) is mounted on a lab stand. Fine adjustment is not required for this camera since it is used primarily to ensure that the plates are parallel and determine how much (if any) the droplet has moved away from the front camera. Both cameras are mounted on custom holders.

gently brought into contact using the z-stage. The custom-built holder is attached to a thick post (Thorlabs, 300 mm post) to hold the entire unit steady as measurements are taken. An optional horizontal stage (Thorlabs, PT1/M—25.0 mm translation stage) can be used for shearing experiments (not used in this paper).

The main camera (IDS, UI-5880CP Rev. 2 GigE CMOS camera^{55,56}) takes a video of the capillary bridge during the stretching experiment at 5 fps (or higher as required). It is focused so as to track accurately the edges of the CLB and angled with respect to the plates to get a good view of the top contact angle and the bridge reflection. The reflection provides a convenient way of determining the position of the surface contact accurately. Since experiments are conducted using identical contacting surfaces, tracking the bridge geometry at its top interface is sufficient to derive all the meaningful parameters for modeling in the absence of gravitational effects. The images from the video are time-stamped for synchronization with the force sensor data and subsequently post-processed using

a bespoke python script to automatically extract the contact angles and radii of curvatures (see Sec. IV).

An optional secondary camera (Dino-lite AM7915MZT—EDGE, Almere, The Netherlands) offers a synchronized side view of the CLB. It is primarily used for measuring the initial plate separation but can also be used to track droplet movement in the transversal direction to the plane imaged by the main camera. This is useful to monitor possible lateral motion of the CLB (and if necessary, bring suitable corrections) and to ensure that the radii measured are correct. The second camera also helps in identifying pinning events missed by the primary camera while working with standard surfaces. From both cameras, the diameter and the surface curvature of the droplet can be accurately quantified for each frame during post-processing.

All the hardware components of the setup interface with LabVIEW, where a bespoke program controls their movement and collects all the data synchronously to ensure accurate

timestamping of each component (see Sec. 2 of the [supplementary material](#)). The choice of using LabVIEW is motivated by the fact that it easily interfaces with the control software of most instruments, and many companies provide dynamic-link library (dll) and driver files such that the full capacity of all the instruments can be utilized without the need for machine-level programming.

The entire setup is placed in a Perspex box (custom built) with an anti-vibration stand (Thorlabs, B4560A—Nexus Breadboard) to prevent environmental changes from affecting the measurements. The Perspex box and the anti-vibration table shield the delicate force sensor from uncontrolled environmental effects and reduce the noise in the system. The box also allows for the local environment (temperature and humidity) to be controlled around the capillary bridge.

2. Measurement protocol

In a standard CLB stretching or compression experiment, the measurements are conducted as follows:

1. The two surfaces of interest are prepared on circular glass coverslips (Agar Scientific, 24 mm) and glued onto a custom-built thin metal mount using fast curing air dry glue (Reprorubber Thin Pour, Bowers Group, Camberley, UK). After 2 hours of curing, the surfaces and metal mounts are screwed into place in the static baseplate and the force sensor of the setup. The whole setup is then left to equilibrate for an hour before the measurements begin.
2. The camera and the light source are adjusted to ensure suitable visualization of the CLB for the desired experimental conditions.
3. The force sensor may be zeroed to remove the offset due to the weight of the sample and mount. For measurements where only the change of force is of interest, the system offset can simply be removed at the stage of data processing, leaving relative force measurements.
4. A droplet is placed onto the lower plate and brought gently into contact with the force sensor.
5. The force sensor and the camera begin recording data. The measurement effectively commences approximately 1–2 mins after the first contact, to allow the force sensor to be fully at equilibrium before starting to collect meaningful data.
6. The stage can be set to move at a particular velocity and over a particular distance.
7. The stage can be set to repeat the stretching/compression motion as required.
8. After completion of the experiment, the timestamped data from each instrument are outputted as a text file (force) or a video file (camera) for post-processing.
9. The data are passed onto a python script for semi-automated post-processing and extraction of the geometrical parameters.

3. Software and data analysis

All the code for data acquisition and processing is available in Secs. 2 and 3 of the [supplementary material](#). A brief description is also given below.

Setup control: Development of a LabVIEW setup to control the different pieces of equipment is relatively straightforward and based on the dll files provided by the different manufacturers or existing LabVIEW modules. The software controls the motion of the different stages (vertical, lateral, and tilt angle) as well the cameras and the data acquisition with timestamping.

Data analysis: All the automated data analysis of the images captured by the cameras is carried out by custom-made procedures programmed in Python. The procedure uses canny edge detection to obtain the silhouette of the bridge. By adjusting the two key detection parameters (minVal and maxVal), the number of edges detected can be increased or decreased to capture just the relevant image information. Constraints are added to the system to filter any features that could impede measurements. From these edge values, a second order polynomial curve is fitted to each side of the bridge. The curvature and gradient at each point of the edge are obtained from the first and second derivative of the quadratic polynomial fit, respectively. The gradient at the contact point with one of the plates is used to calculate the contact angle, while the corresponding

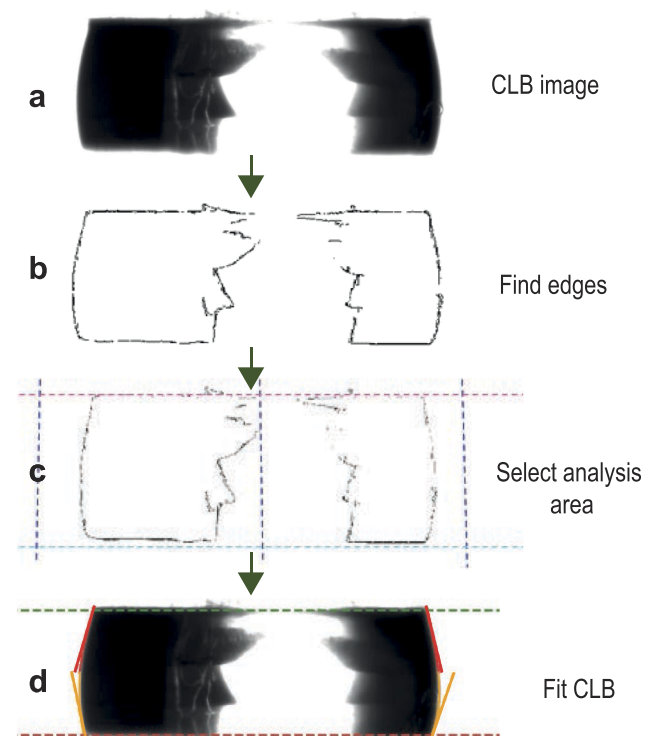


FIG. 4. Flow diagram representation of the analysis process using a bespoke Python routine. Videos of droplet stretching are separated into frames, and each frame is analyzed in turn. The edges of the bridge are detected using canny edge detection, and an adjustable region of interest is selected. By selecting a region of interest, spurious additions to the images arising from noisy edge detection can be removed. The user then defines where the initial top and bottom of the bridge are, allowing for the contact angles and the different radii to be calculated. This process is repeated for each frame, with the software tracking the moving edges as the CLB expands.

curvature, K , is calculated using⁵⁷

$$K = \frac{\left| \frac{d^2 y}{dx^2} \right|}{\left(1 + \left(\frac{dy}{dx} \right)^2 \right)^{3/2}}. \quad (5)$$

The radius of curvature R_2 (see Fig. 1) along the bridge side is simply the inverse of K in Eq. (5). Using the intercept of the lines with the top and bottom plates and similar triangles determines the radii (R_t and R_b , see Fig. 1) of the CLB at the top and bottom. The radius of curvature R_1 (see Fig. 1) can then be calculated using $\frac{1}{R_1} = \frac{\sin \theta_t}{R_t}$ and $\frac{1}{R_1} = \frac{\sin \theta_b}{R_b}$ for the top and bottom plates, respectively. The process is shown schematically in Fig. 4.

Depending on the set of data, the analysis procedure may occasionally fail to extract properly the geometrical parameters due to a variety of external factors, such as unfavorable light reflections and intensity or a particular positioning of the CLB. This typically translates as large, unjustified variations of the parameters between consecutive images (in particular, in the contact angle and radius of curvature). If this occurs, a pre-processing step may be needed whereby certain image features or frames are removed by hand to assist in the edge detection. The fitting area may also be decreased to remove features close to the bridge edge that may interfere with the detection.

4. Comparing measured and calculated forces

In an ideal experiment, the measured and calculated forces would be exactly the same. In reality, however, we usually find that the force sensor has a small but measurable constant offset (typically 20 μN) when compared to the forces calculated from the CLB geometrical parameters using Eq. (1) (Fig. 5). While negligible for measurements involving solid surfaces, this offset needs to be taken into account when comparing calculated and measured forces with the CLB between LIS. Practically, the experimental offset value is

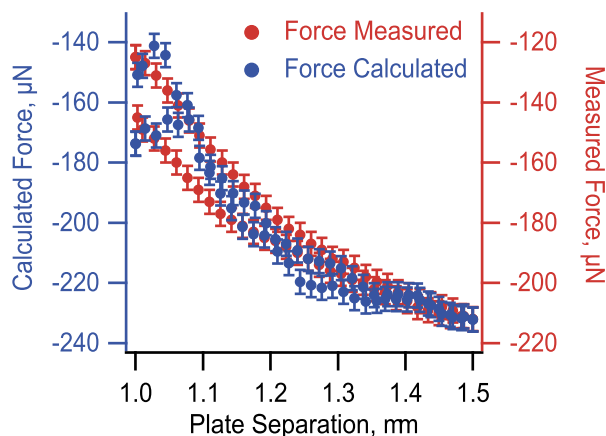


FIG. 5. Example of force offset between the measured (red) and calculated forces (blue). The datasets have been aligned vertically using least square minimization, and the force values associated with each dataset are presented separately (left and right vertical axes). From the differences in the axis values, we deduce an offset of $\sim 20 \mu\text{N}$ between the measured and calculated forces. The uncertainties represent the standard error on the measurements.

quantified in an objective and systematic manner for a given dataset by fitting the experimental data to the calculated data (least squares error minimization for the whole set). The process is illustrated in Fig. 5, where both experimental and calculated forces are given for an aligned set of data. This procedure was carried out systematically thereafter, and the data are displayed with the offset removed from the experimental measurement so as to allow better comparison of the absolute force values. The origin of the offset may be due a variety of factors and appears to depend on the day and type of measurement conducted. This suggests that it could result from daily variation in the load cell calibration due to external parameters (temperature and humidity) or due to the position of the CLB during its setup. However, given its small offset value, the fact that it is constant over a set of data, and the possibility to compensate for it, we do not see this as a major issue.

5. Example of successful measurement

To illustrate the capabilities of the setup, we conducted some CLB measurements with surfaces composed of hydrophobic dimethyldichlorosilane-treated glass (DMS glass) and with LIS. The DMS glass was prepared by vapor deposition as described in Ref. 58. The LIS were prepared following an established protocol as described elsewhere⁵⁹ and had an oil layer thickness of $\sim 6 \mu\text{m}$ to limit oil ridge effects. During a measurement, the CLB is first extended by increasing the distance between the surfaces and subsequently returns to its initial position. The results are compared in Fig. 6, showing a good agreement between the measured and calculated forces derived from the CLB geometry. Movies of both experiments are available in Sec. II of the [supplementary material](#).

Figure 6 illustrates the capabilities of the setup developed: both DMS glass and LIS induce a similar contact angle for the CLB and both bridges have similar dimensions, but the force variation while stretching experienced in both cases differ by a factor of ~ 5 . As expected, the contact angle hysteresis is much lower for LIS compared to DMS glass. This can be seen in the videos in SM2 of the [supplementary material](#), which shows that when the contact line of the CLB on LIS is highly mobile while pinning is often seen for the DMS glass.

C. Troubleshooting and limitations

1. Force sensor considerations

The force sensor is based on a load cell and is hence unavoidably affected by time dependent creep.⁶⁰ In practice, this means that rapid changes to the CLB geometry take several seconds to equilibrate in the associated force measurement. This should be taken into consideration while performing measurements with this setup because it imposes a limitation on the measurable CLB stretching and compressing velocities. We acquired the data shown at relatively slow stretching/compressing velocities (less than 0.01 mm/s), which provided a good agreement between the measured and calculated force values [Fig. 7(a)]. In contrast, the same measurement repeated ten times faster (stretched/compressed at 0.1 mm/s) results in a significant deviation between the measured and calculated forces [Fig. 7(b)]. The measured force becomes affected by a convolution with a time dependent creep, artificially lowering the value of the measured force and preventing equilibrium measurement.

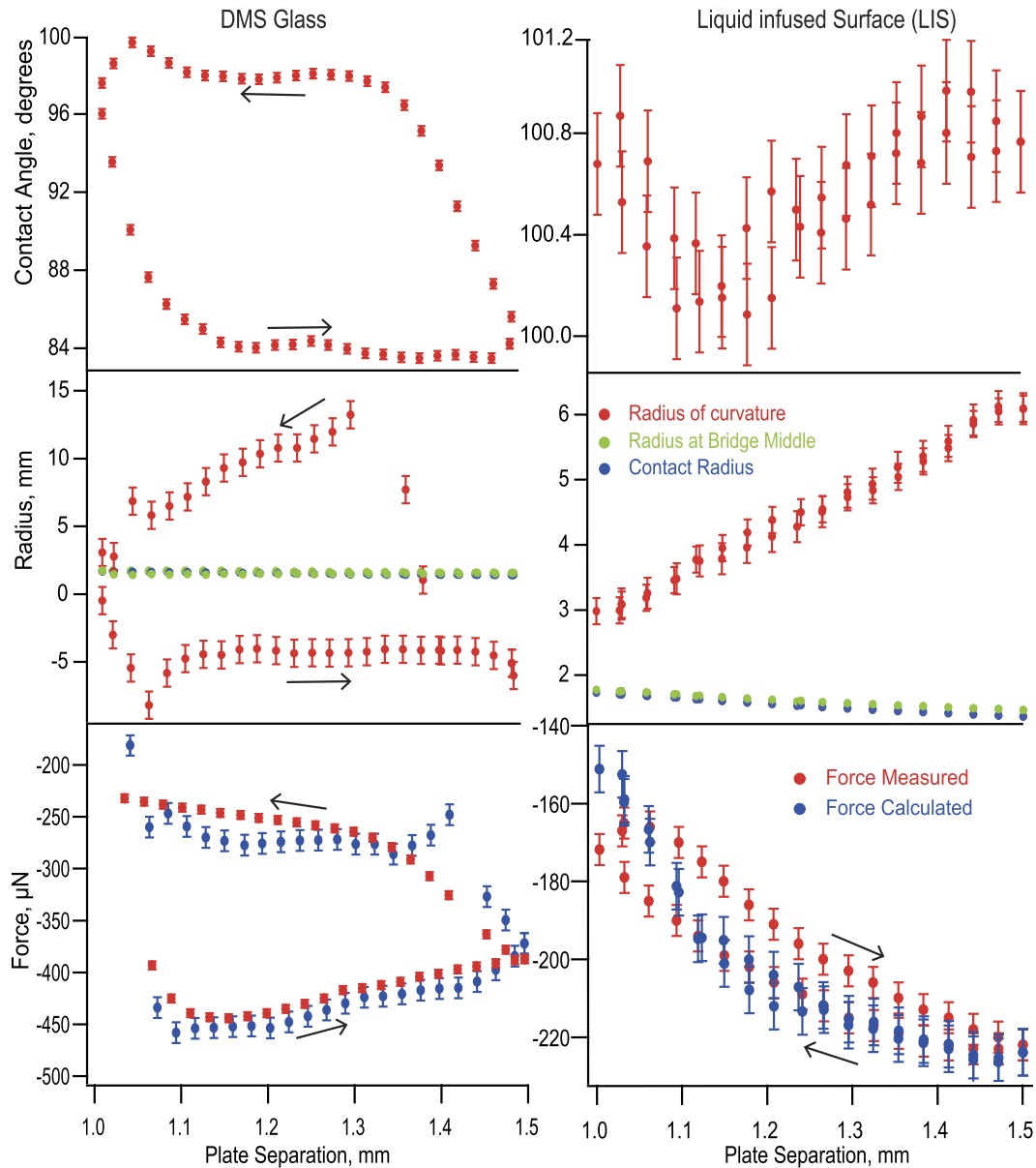


FIG. 6. Comparative CLB measurements conducted on hydrophobized DMS glass (left) and LIS (right). The CLB contact angle with the top plate (top), contact and curvature radii (middle), and force (bottom) are shown. The variation in capillary forces is measured experimentally (red) and calculated using Eq. (2) based on the CLB geometrical parameters (blue). Note the difference in magnitude of the vertical scales between both experiments. Arrows indicate the measurement progression with time. The error bars represent the standard error on the measurements and may occasionally be too small to be seen. The data presented are compensated for the experimental offset (Fig. 5).

2. Bridge pinning

Another interesting feature that can be explored is the pinning of CLBs on solid surfaces. The force is measured globally for the entire bridge and is, therefore, always sensitive to pinning, which often appears as an unexpected force evolution and a deviation from

the theory (Fig. 8). Such pinning is, however, not always visible with the camera. This is because the camera effectively captures only a 2D projection of the 3D CLB, which can create some difficulty for interpreting the results. By adjusting the side camera so that it can visualize the whole triple line of the CLB, it is possible to determine where pinning likely occurred (Fig. 8).

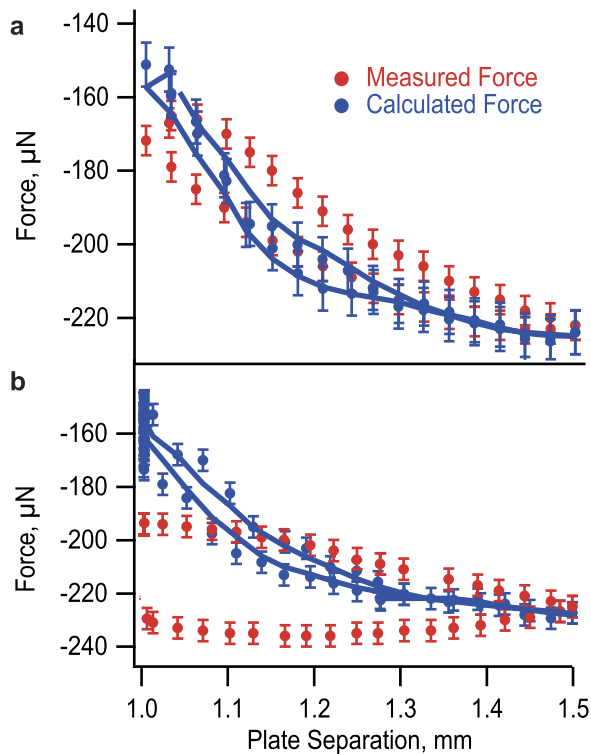


FIG. 7. Effect of the load-cell time dependent creep on measurements. (a) When enough time is allowed by the cell to relax between consecutive measurements, a good agreement is found between the measured and calculated forces. Here, the stretching/compression is conducted at a velocity of 0.008 mm/s. (b) Increasing the velocity by more than an order of magnitude to 0.1 mm/s makes creep effects appear with a significant difference between measured and calculated forces. This is most obvious when reversing the direction of motion, with the measured force being artificially lowered on the return journey. Both plots show the measured (red) and calculated (blue) forces. Equation (2) was used with a 4 pts moving average applied (blue line). Error bars are the standard error for both measurements.

3. Oil ridges for CLBs on LIS

Oil ridges can arise on LIS with a thick surface oil layer. Experimentally and for the type of LIS used here, this typically occurs when the oil layers exceed 12–14 μm (Fig. 9). The ridge appears as an obscured region where the CLB contacts the LIS' surface; ridges are mobile and can grow during measurements. The presence of ridges leaves a smaller region for fitting the CLB's edge. To some extent, this can be mitigated by adapting the analysis software so that it takes into account the entire bridge to extract the geometrical parameters rather than only the region near the top of the oil ridge (see Sec. 3 of the [supplementary material](#)).

III. DISCUSSION AND CONCLUSION

The measurement setup developed in this paper is designed to overcome the difficulties associated with studying CLBs between LIS. It also provides a modular set of components that offers flexibility with the ability to conduct many different types of CLB investigations. The key features of the setup are the integrated

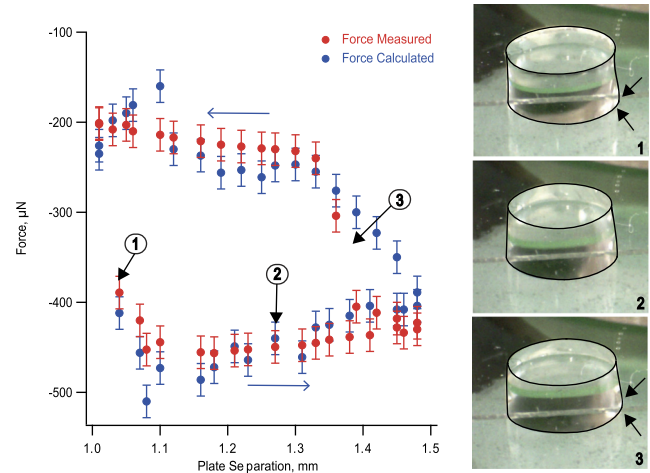


FIG. 8. Example of pinning as detected by the setup for a CLB between surfaces of DMS glass. Image 1, 2, and 3 (top) highlight the CLB at different times during the extension/recovery cycle. Images 1 and 3 correspond to instances of pinning (arrows) during the extension and return, respectively. The pinning visually deforms the CLB, which becomes asymmetrical. Image 2 is an example of the CLB while unpinned during the cycle. If the pinning is clearly visible in the image used for the geometrical analysis of the CLB (Image 1), the measured and calculated forces tend to coincide. However, if the pinning occurs out of focus to the imaging plane, it may be missed out or only partially captured (image 3), resulting in a sharp deviation between the measured and calculated forces. The measured (red) and calculated [blue, using Eq. (2)] are shown. The offset between the two force curves has been removed, as detailed in Fig. 5.

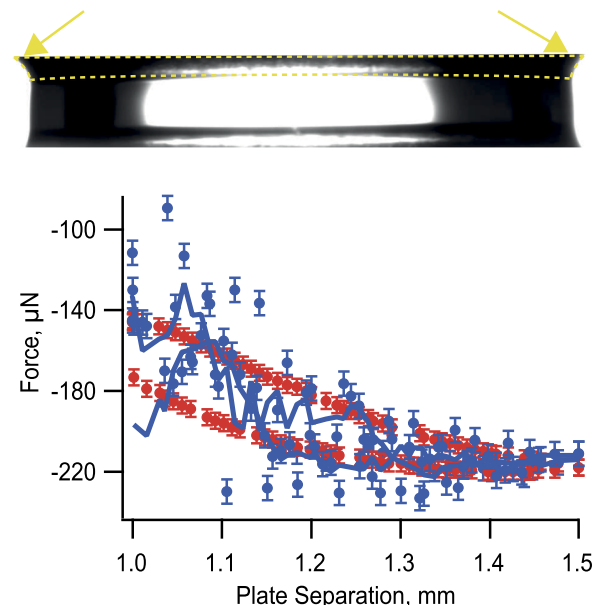


FIG. 9. Example of CLB measurement in the presence of an oil ridge. The oil ridge (dotted outline and arrows, top) renders the extraction of the contact angle and CLB radii at the top plate more challenging. By adjusting the fitting region used for the CLB's edge, a better approximation can be achieved, but the calculated force (blue, bottom plot) remains considerably noisier than the measured force (red). A 4 pts moving average of the calculated force Eq. (2) is also given (blue line). The error bars represent the standard error of the measurements.

measurement of all variables, the high sensitivity of the force sensor, and the custom-built analysis software to extract the relevant information from the experimental data.

The force measurement is sensitive enough to quantify the small force variations associated with experiments on LIS and could also be used to probe force variations associated with smaller liquid bridge deformations on conventional surfaces. The data can then be processed to high temporal accuracy with up to 20 images per second and 10 force sensor readings per second. Care must be taken to ensure that measurements are not affected by time dependent creep. While unavoidable in load cells, it can be mitigated by controlling the CLB stretching/compression velocities.

The system, having motorized stages that can move in all three directions (x, y, and z), is not limited to the simple stretching experiments shown here but can also perform shearing experiments or combinations of thereof. The position of the stages can be controlled with 0.1 μm accuracy, if necessary. The isolation of the setup in a Perspex box allows for control of the local environment around the CLB (e.g., humidity or temperature).

The accuracy of the calculations is currently limited by several factors. First, there is only one projection from which to measure the droplet geometry at any given time. Adding a second or third camera with a similar resolution could significantly improve the analysis by offering an average picture of the CLB and help identify pinning events. The camera themselves can also be improved to avoid limitations inherent to the number of pixels available for the data analysis. This can be easily addressed by upgrading the camera with a model that has higher speed and resolution. The orientation of the cameras can also be readily adapted to view the footprint of the CLB or a side view depending on the needs of the experiment.

Finally, the flexibility of the setup makes it an ideal tool to adapt to different types of systems. With measurements involving LIS, for example, large extensions can lead to higher droplet mobility and a smaller signal on the force sensor. Hence, a compromise has to be found in order to achieve repeatable measurements. For longer sets of measurements, using a glycerol solution instead of water reduces evaporation to a workable level over the timescales of the experiment.

In conclusion, we propose a fully motorized setup to track the characteristics of CLBs between any two surfaces of interest. The setup is relatively inexpensive, comparable to the cost of an analytical balance. Its configuration is flexible, and it is particularly suitable for measurements where a high force sensitivity is required.

SUPPLEMENTARY MATERIAL

The [supplementary material](#) contains two video files of the example successful measurements (description is available in Sec. SM1), the LabVIEW scripts for operating the setup and capturing the data (Sec. SM2), and the Python scripts for the data analysis (Sec. SM3).

ACKNOWLEDGMENTS

The authors would like to thank Gary Wells for his advice on equipment purchase and 3D printing components. They would also like to thank the electronic and mechanical workshops in the

Department of Physics for creating and advising on many of the custom parts mentioned in the text. S.J.G. gratefully acknowledges the EPSRC for funding through the SOFI (Soft Matter and Functional Interfaces) Center for Doctoral Training (Grant No. EP/L015536/1).

AUTHOR DECLARATIONS

Conflict of Interest

The authors have no conflicts to disclose.

Author Contributions

S.J.G., H.K., and K.V. designed the experiments. S.J.G. performed all the measurements. S.J.G. analyzed the results with help from H.K. and K.V. S.J.G., H.K., and K.V. wrote the paper.

DATA AVAILABILITY

The data that support the findings of this study are available from the corresponding authors upon reasonable request.

REFERENCES

- D. J. Hornbaker, R. Albert, I. Albert, A.-L. Barabási, and P. Schiffer, *Nature* **387**, 765 (1997).
- M. Li, L. Shi, and X. Wang, *Colloids Surf., B* **199**, 111531 (2021).
- B. N. J. Persson, *J. Phys.: Condens. Matter* **19**, 376110 (2007).
- W. Federle, M. Riehle, A. S. G. Curtis, and R. J. Full, *Integr. Comp. Biol.* **42**, 1100 (2002).
- T. M. Tamer, *Interdiscip. Toxicol.* **6**, 111 (2013).
- S. Bian, C.-F. Tai, D. Halpern, Y. Zheng, and J. B. Grotberg, *J. Fluid Mech.* **647**, 391 (2010).
- M. Heil, A. L. Hazel, and J. A. Smith, *Respir. Physiol. Neurobiol.* **163**, 214 (2008).
- M. Makrygianni, E. Margariti, K. Andritsos, D. Reppas, F. Zacharatos, N. Oikonomidis, C. Spandonidis, and I. Zergioti, *J. Laser Micro. Nanoeng.* **15**, 204 (2020).
- G. Schouten, *Circuit World* **14**, 41 (1988).
- H. Wang, X. Li, K. Luan, and X. Bai, *RSC Adv.* **9**, 23986 (2019).
- M. D. Zoback and A. H. Kohli, *Unconventional Reservoir Geomechanics: Shale Gas, Tight Oil, and Induced Seismicity* (Cambridge University Press, 2019).
- T. Zhou, K. Ioannidou, F.-J. Ulm, M. Z. Bazant, and R. J.-M. Pellenq, *Proc. Natl. Acad. Sci. U. S. A.* **116**, 10652 (2019).
- J. Kim, B. Guenthart, J. D. O'Neill, N. V. Dorrello, M. Bacchetta, and G. Vunjak-Novakovic, *Sci. Rep.* **7**, 13082 (2017).
- A. C. M. Shek, C. Semperebon, J. R. Panter, and H. Kusumaatmaja, *Langmuir* **37**, 908 (2021).
- G. E. Valenzuela, *J. Phys. Chem. C* **123**, 1252 (2019).
- E. Sahagún, P. García-Mochales, G. M. Sacha, and J. J. Sáenz, *Phys. Rev. Lett.* **98**, 176106 (2007).
- M. H. Korayem, A. Kavousi, and N. Ebrahimi, *Sci. Iran.* **18**, 121 (2011).
- E. J. De Souza, M. Brinkmann, C. Mohrdieck, A. Crosby, and E. Arzt, *Langmuir* **24**, 10161 (2008).
- A. Fukunishi and Y. Mori, *Adv. Powder Technol.* **17**, 567 (2006).
- M. Farshchi-Tabrizi, M. Kappl, Y. Cheng, J. Gutmann, and H.-J. Butt, *Langmuir* **22**, 2171 (2006).
- C. D. Willett, M. J. Adams, S. A. Johnson, and J. P. K. Seville, *Langmuir* **16**, 9396 (2000).
- Z. Shi, Y. Zhang, M. Liu, D. A. H. Hanaor, and Y. Gan, *Colloids Surf., A* **555**, 365 (2018).
- F. Xiao, J. Jing, S. Kuang, L. Yang, and A. Yu, *Powder Technol.* **363**, 59 (2020).
- D. J. Broesch and J. Frechette, *Langmuir* **28**, 15548 (2012).
- E. Reyssat, *J. Fluid Mech.* **748**, 641 (2014).

- ²⁶Y.-C. Liao, E. I. Franses, and O. A. Basaran, *Phys. Fluids* **18**, 022101 (2006).
- ²⁷Y.-C. Liao, H. J. Subramani, E. I. Franses, and O. A. Basaran, *Langmuir* **20**, 9926 (2004).
- ²⁸H. Chen, T. Tang, and A. Amirfazli, *Soft Matter* **10**, 2503 (2014).
- ²⁹D. N. Mazzone, G. I. Tardos, and R. Pfeffer, *J. Colloid Interface Sci.* **113**, 544 (1986).
- ³⁰D. Tian, Y. Song, and L. Jiang, *Chem. Soc. Rev.* **42**, 5184 (2013).
- ³¹Z. Wang and Y.-P. Zhao, *Phys. Fluids* **29**, 067101 (2017).
- ³²V. Liimatainen, M. Vuckovac, V. Jokinen, V. Sariola, M. J. Hokkanen, Q. Zhou, and R. H. A. Ras, *Nat. Commun.* **8**, 1798 (2017).
- ³³T.-S. Wong, S. H. Kang, S. K. Y. Tang, E. J. Smythe, B. D. Hatton, A. Grinthal, and J. Aizenberg, *Nature* **477**, 443 (2011).
- ³⁴A. Lafuma and D. Quéré, *Europhys. Lett.* **96**, 56001 (2011).
- ³⁵S. Peppou-Chapman, J. K. Hong, A. Waterhouse, and C. Neto, *Chem. Soc. Rev.* **49**, 3688 (2020).
- ³⁶T. Yamazaki, M. Tenjimabayashi, K. Manabe, T. Moriya, H. Nakamura, T. Nakamura, T. Matsubayashi, Y. Tsuge, and S. Shiratori, *Ind. Eng. Chem. Res.* **58**, 2225 (2019).
- ³⁷Y. H. Yeong, C. Wang, K. J. Wynne, and M. C. Gupta, *ACS Appl. Mater. Interfaces* **8**, 32050 (2016).
- ³⁸P. Kim, T.-S. Wong, J. Alvarenga, M. J. Kreder, W. E. Adorno-Martinez, and J. Aizenberg, *ACS Nano* **6**, 6569 (2012).
- ³⁹J. Li, T. Kleintschek, A. Rieder, Y. Cheng, T. Baumbach, U. Obst, T. Schwartz, and P. A. Levkin, *ACS Appl. Mater. Interfaces* **5**, 6704 (2013).
- ⁴⁰C. Howell, A. Grinthal, S. Sunny, M. Aizenberg, and J. Aizenberg, *Adv. Mater.* **30**, 1802724 (2018).
- ⁴¹G. Shi, Y. Wang, S. Derakhshanfar, K. Xu, W. Zhong, G. Luo, T. Liu, Y. Wang, J. Wu, and M. Xing, *Mater. Sci. Eng. C* **100**, 915 (2019).
- ⁴²M. Zhang, Q. Liu, J. Liu, J. Yu, and J. Wang, *MRS Commun.* **9**, 92 (2019).
- ⁴³M. Tenjimabayashi, S. Nishioka, Y. Kobayashi, K. Kawase, J. Li, J. Abe, and S. Shiratori, *Langmuir* **34**, 1386 (2018).
- ⁴⁴M. Liu, Y. Hou, J. Li, L. Tie, and Z. Guo, *Chem. Eng. J.* **337**, 462 (2018).
- ⁴⁵P. V. Petkov and B. Radoev, *Colloids Interfaces* **3**, 68 (2019).
- ⁴⁶H. Kusumaatmaja and R. Lipowsky, *Langmuir* **26**, 18734 (2010).
- ⁴⁷X. Lin, W. Ma, L. Chen, L. Huang, H. Wu, and A. Takahara, *RSC Adv.* **9**, 34465 (2019).
- ⁴⁸H. K. Cammenga, F. W. Schulze, and W. Theuerl, *J. Chem. Eng. Data* **22**, 131 (1977).
- ⁴⁹L. Lecoq, D. Flick, and O. Laguerre, *Int. J. Therm. Sci.* **111**, 450 (2017).
- ⁵⁰J. Qu, L. Escobar, J. Li, Z. Rao, and B. Xu, *Int. Commun. Heat Mass Transfer* **110**, 104427 (2020).
- ⁵¹D. Daniel, J. V. I. Timonen, R. Li, S. J. Velling, and J. Aizenberg, *Nat. Phys.* **13**, 1020 (2017).
- ⁵²A. Keiser, L. Keiser, C. Clanet, and D. Quéré, *Soft Matter* **13**, 6981 (2017).
- ⁵³A. A. Günay, S. Sett, Q. Ge, T. Zhang, and N. Miljkovic, *Adv. Mater. Interfaces* **7**, 2000983 (2020).
- ⁵⁴F. Schellenberger, J. Xie, N. Encinas, A. Hardy, M. Klapper, P. Papadopoulos, H.-J. Butt, and D. Vollmer, *Soft Matter* **11**, 7617 (2015).
- ⁵⁵M. S. Sadullah, G. Launay, J. Parle, R. Ledesma-Aguilar, Y. Gizaw, G. McHale, G. G. Wells, and H. Kusumaatmaja, *Commun. Phys.* **3**, 166 (2020).
- ⁵⁶S. Armstrong, G. McHale, R. Ledesma-Aguilar, and G. G. Wells, *Langmuir* **35**, 2989 (2019).
- ⁵⁷M. Do Carmo, *Differential Geometry of Curves and Surfaces* (Dover Publications, 1976).
- ⁵⁸R. Deng, L. Yang, and C. D. Bain, *ACS Appl. Mater. Interfaces* **10**, 12317 (2018).
- ⁵⁹S. J. Goodband, S. Armstrong, H. Kusumaatmaja, and K. Voitchovsky, *Langmuir* **36**, 3461 (2020).
- ⁶⁰T. W. Bartel and S. L. Yaniv, *J. Res. Natl. Inst. Stand. Technol.* **102**, 349 (1997).